Effect of $LiClO_4$ on the Structure and Mobility of PEO-Based Solid Polymer Electrolytes

Susan K. Fullerton-Shirey and Janna K. Maranas*

Department of Chemical Engineering, The Pennsylvania State University, University Park, Pennsylvania 16802

Received November 7, 2008; Revised Manuscript Received January 20, 2009

ABSTRACT: The relationship between structure, PEO mobility, and ionic conductivity is investigated for the solid polymer electrolyte, PEO/$LiClO_4$. Amorphous and semicrystalline samples with ether-oxygen-to-lithium ratios ranging from 4:1 to 100:1 are measured. Previous X-ray diffraction results show that three crystalline phases can form in this system depending on the $LiClO_4$ concentration: $(PEO)_3$:$LiClO_4$, pure PEO, and $(PEO)_6$:$LiClO_4$. We use SANS to determine that the $(PEO)_3$:$LiClO_4$ phase forms cylinders with a radius of 125 Å and a length of 700 Å. We also measure the amount and size of pure PEO lamellae by exploiting the neutron scattering length density contrast that arises because of crystallization. The samples are thermally treated such that the $(PEO)_6$:$LiClO_4$ phase does not form. QENS is used to measure PEO mobility directly in amorphous and semicrystalline samples, and it reveals two processes. The first process at short times is attributed to the segmental mobility of PEO, and the second process at longer times is attributed to the restricted rotation of protons around the Li^+ ions. The type of motion and the radius of rotation are consistent with a cylindrical structure observed by diffraction: two PEO chains wrapping around Li^+ ions in an ether-oxygen-to-lithium ratio of 6:1. By directly comparing structure, mobility, and conductivity of the same samples, we determine that at 50 °C, a semicrystalline sample (concentration of 14:1) has the highest conductivity despite being less mobile, partially crystalline, and having less charge carriers than amorphous samples at the same temperature. The results suggest a decoupling of ionic conductivity and polymer mobility.

Introduction

The liquid-phase electrolytes currently used in rechargeable lithium-ion batteries restrict battery design flexibility and create end-of-life disposal issues. Replacing the liquid with a solid electrolyte would eliminate the need for a rigid battery casing, permitting the design of a flexible battery. Furthermore, if the solid-state material was nontoxic, then end-of-life disposal issues would be reduced. As a result, effort has been ongoing to replace the liquid electrolyte with a polymer, namely polyethylene oxide (PEO) plus a lithium salt. PEO is chosen because it is nontoxic, has a flexible backbone, and can solvate ions. However, the rate at which the lithium ions move at room temperature is low, resulting in conductivity that is insufficient for practical application.

PEO-based solid polymer electrolytes (SPEs) have a rich phase behavior that depends on the temperature, lithium concentration, thermal history, and anion identity. In a semicrystalline sample, the crystalline domains can contain more than one phase, as illustrated in Figure 1 for PEO/$LiClO_4$, where crystalline complexes of $(PEO)_6$:$LiClO_4$, $(PEO)_3$:$LiClO_4$ and pure PEO can form.[1] (We will indicate SPE systems with a "/" and crystalline complexes with a ":" between the polymer and the salt.) The melting point of the $(PEO)_6$:$LiClO_4$ complex varies between 50 and 65 °C depending on the lithium concentration, whereas the $(PEO)_3$:$LiClO_4$ complex melts at a higher temperature (150 °C at an ether-oxygen-to-lithium ratio (EO/Li) of 4:1). Above the melting point, the SPE is fully amorphous, and the lithium ions (Li^+) are coordinated with multiple ether oxygens on the PEO chain. The number of coordinating ether oxygen atoms depends on the lithium concentration and the identity of the anion and can be predicted with knowledge of the crystalline structures. Specifically, the extent of coordination in the amorphous phase corresponds to the coordination of the crystalline complex that will form as the temperature is lowered.

* Corresponding author. E-mail: jmaranas@engr.psu.edu.

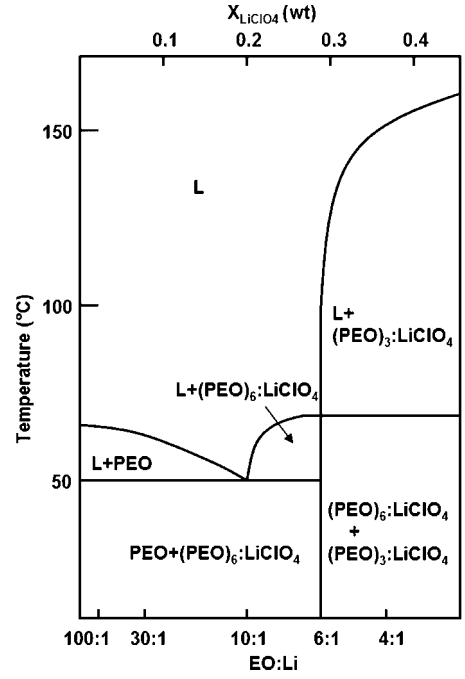

Figure 1. Phase diagram for PEO/$LiClO_4$ reproduced from ref 1. EO:Li represents the ratio of PEO ether oxygens to lithium ions.

Examples of this coordination are provided in Table 1 for several SPEs. In the case of LiI, $(PEO)_3$:LiI is the only lithium-containing crystalline complex that forms regardless of lithium concentration,[2] whereas multiple lithium-containing crystalline complexes can form in PEO/$LiClO_4$[1] and PEO/LiTFSI.[3,4] One feature that the SPEs have in common is the existence of a eutectic point near a concentration of 11:1 (Table 1). In the case of PEO/LiTFSI made with low-molecular-weight PEO (4000 g/mol), a eutectic point is not observed. Instead, a

10.1021/ma802502u CCC: $40.75
Published on Web 02/23/2009

Table 1. EO:Li Coordination For Several SPEs[a]

	coordination (EO:Li)			
SPE system	overall	crystalline	amorphous	eutectic point
$PEO/LiClO_4$	7.5:1	6:1[1]	4−5:1[6]	10:1[1]
PEO/LiTFSI	7.5:1	6:1[3,4]	5:1[7]	11:1[3,4]
PEO/LiI	5:1	3:1[2]	3.5:1[8]	11.5:1[2]

[a] The amorphous coordination can be predicted on the basis of this crystalline coordination. (TFSI stands for $N(SO_2CF_3)_2$).

"crystallization gap" occurs at EO:Li concentrations ranging from 12:1 to 6:1.[5]

Lithium ions move through amorphous domains by making and breaking complexes with ether oxygen atoms. The mobility of Li^+ is facilitated by the segmental relaxation of the polymer host. Consequently, efforts to improve conductivity have mainly focused on increasing polymer mobility in the amorphous phase. The mobility of fully amorphous SPEs has been reported using quasi-elastic neutron scattering (QENS) for the following systems and concentrations: PEO/LiI (15:1, 20:1),[9] $PEO/LiClO_4$ (8:1),[10] PEO/LiTFSI (8:1),[10] and PEO/LiBETI (15:1, 20:1),[11] where BETI stands for $N(SO_2C_2F_5)_2$. The segmental mobility of PEO decreased for all SPEs with the addition of lithium salt. The extent of the decrease depends on lithium concentration, anion identity, and temperature. It is reasonable to expect the dynamics of the polymer to decrease with the addition of $LiClO_4$ because multiple ether oxygen atoms coordinate with Li^+, thereby restricting the mobility of PEO. In the case of PEO/LiTFSI[10] and PEO/LiBETI,[11] not only were PEO segmental dynamics slowed with the addition of lithium but also a second process appeared on the time scale of the measurement. The origin of the extra process is attributed to the formation and disruption of "cross-links" between Li^+ and ether oxygen atoms. Both systems have an ether-oxygen-to-lithium ratio of approximately 6:1 in the amorphous phase at the lithium concentrations measured in the QENS studies. This coordination has been measured by neutron diffraction for PEO/LiTFSI (Table 1) and is predicted for PEO/LiBETI on the basis of the 6:1 crystalline complex that would form at overall concentrations of 15:1 and 20:1.[12] Unlike PEO/LiTFSI and PEO/LiBETI, QENS measurements on LiI revealed only one dynamic process, with the scattering function decaying fully during the time scale of the measurement (1000 ps).[9] Only one process was observed for $PEO/LiClO_4$ as well; however, the time scale of the measurement extended to only 100 ps.[10] The scattering function did not fully decay in this sample; a fraction of the sample remained static. It is possible that only one process exists in the case of $PEO/LiClO_4$ or that the second process occurs on time scales longer than the measurement.

While many studies have focused on increasing conductivity by increasing polymer mobility, the belief that Li^+ transport occurs most effectively through amorphous domains has been challenged. For example, a crystalline SPE prepared with low-molecular-weight PEO (1000 g/mol) and $LiSbF_6$ with an ether-oxygen-to-lithium ratio of 6:1 shows greater conductivity than the amorphous equivalent.[13] X-ray powder diffraction data combined with ab initio structure calculations revealed the structure to be pairs of PEO chains forming cylindrical tunnels. Each Li^+ ion is coordinated with six ether oxygens inside the tunnels, and anions are located outside of the tunnels.[14,15] Multiple PEO cylinders align together with a column of anions between. The authors suggest that the static, ordered environment of the crystalline phase is more favorable than the disorganized amorphous phase because directed Li^+ ion transport can occur within the cylinders. SPE complexes of $(PEO)_6$:LiX, where X = PF_6,[16] AsF_6,[13] and TFSI,[17] are reported to share the same cylindrical structure as $(PEO)_6:LiSBF_6$,[16] and the structure is maintained when prepared with high-molecular-weight PEO.[16,18,19] Molecular dynamics simulations of PEO/LiTFSI reveal a slight difference in the structure compared with the experimental results.[17] In the simulations, Li^+ ions are wrapped by two PEO helixes, whereas experimental data suggest two nonhelical interlocking cylinders of PEO surrounding Li^+ ions. In either case, the structure provides a pathway for Li^+ ions to travel.

It is suggested that the cylindrical structure persists to some extent in the amorphous phase. Neutron diffraction of PEO/LiTFSI reveals intermediate-range order near Li^+ ions in the amorphous phase that persists for 20 Å and is reminiscent of the crystalline $(PEO)_6$:LiTFSI complex.[7] A similar observation of intermediate-ranged order has been made for amorphous $PEO/LiClO_4$ using neutron diffraction,[6] although the peak associated with the cylindrical feature is weaker than the peak observed in PEO/LiTFSI.

The molecular weight and the resulting long-range crystalline morphology of PEO plays an important role in Li^+ transport in the 6:1 crystalline complex. This was verified in a study where the molecular weight of PEO in PEO/LiTFSI was doubled from 1000 to 2000 g/mol and the conductivity was decreased as much as five orders of magnitude.[18] The authors suggest that longer PEO chains increase the likelihood that the cylindrical tunnels that direct Li^+ transport will become misaligned. While the conductivity decreases, neutron diffraction shows that the cylindrical structure is maintained at high molecular weight (100 000 g/mol).[13] Because observations on length scales larger than diffraction reveal that $(PEO)_6$:LiTFSI complexes fold into lamellae when high-molecular-weight PEO is used,[20,21] this suggests that the cylindrical structure is retained within the lamellae. Despite fast Li^+ mobility through the cylinders, the long-range lamellar structure does not provide a direct pathway for Li^+ transport, and the conductivity decreases because of the lamellar morphology.

In addition to the $(PEO)_6$:LiTFSI complex, a crystalline complex of $(PEO)_3$:LiTFSI can also form. According to powder diffraction data, the PEO in this phase adopts a helical conformation where Li^+ ions are located within each turn of the PEO chain, and each ion is coordinated with three ether oxygens.[19] Marzantowicz and coworkers demonstrated improved conductivity through this crystalline phase over the amorphous equivalent at low temperature.[21] Similar to $(PEO)_6$:LiTFSI, it is possible that the cylindrical geometry of the $(PEO)_3$:LiTFSI complex provides a pathway for direct Li^+ transport.

In combination, these studies provide evidence of the fact that ionic conductivity can be maintained and even enhanced in crystalline structures, although the macroscopic structure of the SPE must also be considered. This suggests the possibility of developing crystalline-based SPEs with superior conductivity to the amorphous equivalent as long as the conduction pathways percolate over a large spatial scale. Although the idea of conduction through crystalline structures is often dismissed in favor of ion transport in purely amorphous SPEs, the concept of ion transport in crystals and through channels is not new. For example, while solids such as $Li_{0.27}La_{0.59}TiO_3$[22] and sodium β-alumina[23] do not have desirable mechanical properties, their conductivity values (1.5×10^{-3} and 1.4×10^{-2} S/cm at room temperature) are higher than amorphous SPEs despite having fully crystalline structures. An example of transport through channels includes ion channels in cells that regulate the flow of ions across the cell membrane. Another example is Nafion, a polymer with a channel structure that directs the flow of protons in fuel cells.

The observation that high conductivity values can be achieved in the presence of pure PEO crystals and within crystalline complexes challenges the notion that polymer mobility controls conductivity. To determine if dynamics become uncoupled from

Table 2. Heat Treatment Conditions before Each Measurement (Premeasurement), During the Time between Premeasurement and Measurement, and during the Measurement[a]

	premeasurement			intermediate	measurement		
technique	T (°C)	time (h)	environment	time (min) at 22 °C	T (°C)	time (min)	environment
SANS	100	24	vacuum	10	75, 50, 22	60	N_2
QENS	100	24	vacuum	10	75, 50, 22	60	N_2
DCS	100	24	vacuum	10	−90 to 200	N/A	N_2
BDS	100	24	vacuum	30	22 to 100	10	N_2

[a] The premeasurement and measurement times represent how long the sample was held at each temperature reported in the table. The intermediate time represents how long the sample was handled at room temperature between premeasurement and measurement.

conductivity, we measure structure, dynamics, and conductivity in amorphous and semicrystalline SPEs. A decoupling of these variables would support the concept of conduction through or in the presence of crystalline regions. We choose PEO/$LiClO_4$ as our SPE, a system that has been suggested to have crystalline structures similar to those of PEO/LiTFSI.[7] We thermally treat our samples to isolate the pure PEO and $(PEO)_3$:$LiClO_4$ crystalline phases. Crystalline morphology is measured using small-angle neutron scattering (SANS). Although SANS has been used to study SPEs in solution, fewer studies have been performed in the melt state. To our knowledge, this is the first investigation of a semicrystalline SPE investigated in the melt by SANS.

The dynamics of PEO/$LiClO_4$ are measured using QENS as a function of lithium concentration in the amorphous and semicrystalline phases on timescales extending to 2000 ps. Because the scattering will be dominated by the hydrogen atoms in the PEO, we directly measure the mobility of PEO in the presence of $LiClO_4$, requiring no special modification such as deuteration. We measure samples under conditions in which various crystalline phases are present: a sample with an ether-oxygen-to-lithium ratio of 4:1, where the formation of the $(PEO)_3$:$LiClO_4$ structure is expected, and samples with ratios ranging from 14:1 to 100:1, where pure PEO has crystallized. Lithium will be expelled from the pure PEO lamellae, effectively increasing the concentration of lithium in the surrounding amorphous domains. Because we also measure purely amorphous samples over a broad range of lithium concentrations, the effect of lithium concentration can be separated from the effect of crystallinity. The amorphous samples provide information on the influence of $LiClO_4$ concentration alone, whereas the crystalline samples include the effect of crystalline structures on mobility. By comparing these results with conductivity measurements, we can determine if decreased polymer mobility is the only effect of crystallization on conductivity.

We complement SANS and QENS by characterizing the extent of PEO crystallization using differential scanning calorimetry (DSC) and ionic conductivity using broadband dielectric spectroscopy (BDS). During all measurements, we are careful to control variables that can significantly impact the conductivity and crystallization time, such as thermal history and water content.

Experimental Details

Sample Preparation. SPEs were prepared using two types of PEO: commercial PEO from Aldrich (M_w 600 000 g/mol) and a PEO standard from Polymer Standards Services (M_w 500 000 g/mol). We determined that samples made with the commercial PEO gave the same results for QENS and BDS as samples made with the standard PEO. However, because of the presence of micron-sized SiO_2 particles added during the commercial PEO manufacturing, standard PEO was used for SANS because these particles would give rise to a signal in the SANS window and obscure the desired measurement. Samples were prepared with ether-oxygen-to-lithium ratios of 4:1, 8:1, 10:1, 14:1, 30:1, and 100:1. PEO and $LiClO_4$ (Aldrich) were dissolved in anhydrous acetonitrile (Aldrich) and mixed for 24 h in covered Teflon beakers. The lids were removed, allowing the solvent to evaporate while mixing. The material dried in a vacuum oven at 75 °C for 5 days. Samples were hot-pressed at 100 °C to the appropriate thickness for conductivity, SANS, and QENS measurements. Samples were pressed into discs that were ~12 mm in diameter and 0.3 mm thick for BDS and 2.5 cm in diameter and 0.8 mm thick for SANS. The sample thicknesses for the QENS experiments were calculated such that each sample would scatter 10% of the incident neutrons, thereby eliminating the likelihood of multiple scattering events. The average thickness of the QENS samples was 80 μm.

Thermal Treatment. We thermally treat our samples so that pure PEO and $(PEO)_3$:$LiClO_4$ are the only crystalline complexes present. Similar to the $(PEO)_6$:LiTFSI crystalline complex,[20] the $(PEO)_6$:$LiClO_4$ complex does not immediately form. We determined that 3 days is the time required for the $(PEO)_6$:$LiClO_4$ phase to form at room temperature. We determined the time by measuring the 4:1 sample with DSC each day after heating the sample to 100 °C on the first day. We chose this sample because pure PEO does not crystallize at this Li^+ concentration, and the $(PEO)_3$:$LiClO_4$ complex melts at a temperature well above that of the $(PEO)_6$:$LiClO_4$ complex at 4:1. As a result, any feature that arises in the DSC scan near 60 °C represents the $(PEO)_6$:$LiClO_4$ complex. Because we measure our samples within several hours after heating to 100 °C, we do not expect any contribution from the $(PEO)_6$:$LiClO_4$ complex. The only exceptions to this thermal treatment are noted below, where we purposely allow the $(PEO)_6$:$LiClO_4$ complex to form and measure the conductivity and extent of crystallinity. The individual heat treatments are discussed in each section, and a summary is provided in Table 2.

Thermal Analysis and Conductivity Measurements. DSC measurements were made on all samples using a TA Instruments Q1000 DSC calibrated with an indium standard. Sample weights were 8−10 mg, and measurements were performed with a heating rate of 10 °C/min and a cooling rate of 5 °C/min. The PEO crystalline fraction was calculated on the basis of the perfect heat of fusion for PEO, 203 J/g.[24]

BDS was used to measure the ionic conductivity. The samples were placed between two brass electrodes and heated to 100 °C in a vacuum oven to improve contact between the SPE and the electrode. A Teflon spacer was used to maintain the proper diameter and sample thickness. After the samples were removed from the oven, they were held in a desiccator for no longer than 30 min prior to the measurement. Spectra were collected isothermally using a Novocontrol GmbH concept 40 broadband dielectric spectrometer in the frequency range of 1 Hz to 1 MHz for a temperature range of 22−100 °C. The temperature was controlled within 0.2 °C, and the samples were equilibrated at each temperature for 10 min.

Neutron Scattering. Neutron scattering measurements were performed on three instruments at the NIST Center for Neutron Research in Gaithersburg, MD. The NG-3 SANS instrument was used to measure structure, and the dynamics were measured using the disc-chopper time-of-flight spectrometer (DCS) and the high-flux backscattering spectrometer (HFBS). Within a SANS experiment, the coherent contribution gives information on structure, whereas the incoherent contribution adds a structureless background. A difference must exist between the coherent scattering length densities of two species, and this often requires that one species is deuterated. However, as suggested by the X-ray diffraction data used to generate the phase diagram for PEO/$LiClO_4$, the different

salt concentrations in the amorphous and crystalline domains create sufficient contrast so that no special modification is required. Specifically, the contrast arises from the scattering length density difference between PEO/$LiClO_4$ and pure PEO. Weak features can also be resolved in pure semicrystalline PEO as a result of the small density difference between crystalline and amorphous PEO. QENS measures the mobility of atoms in the sample. In the current study, this is dominated by the incoherent scattering of hydrogen atoms, reflecting self-motion of protons rather than the background that incoherent scattering contributes to the SANS measurements. The details of the SANS and QENS measurements are described below.

SANS samples were mounted between two pieces of quartz and sealed in a titanium sample cell under a nitrogen environment. A sample block coupled to a NESLAB circulating bath was use to control the temperature of the samples within 0.1 °C. Samples were measured at three temperatures from highest to lowest (75, 50, and 22 °C), allowing 1 h for thermal equilibration at each temperature. The wavelength of the incident neutron beam was 6 Å. Three sample-to-detector distances were used: 1, 4, and 13 m, covering a spatial range (r) from 21 to 2093 Å. The corresponding scattering vector (q) range is 0.003 to 0.3 $Å^{-1}$, where $q = 2\pi/r$. All data reduction and analysis was performed with the IGOR Pro software using the reduction and analysis macros developed at NIST.[25] The raw data were corrected for scattering from the empty quartz cell, background scattering, detector sensitivity, sample transmission, and sample thickness. The reduced data were circularly averaged, giving the scattered intensity, $I(q)$ versus q.

Samples for the QENS measurements were sandwiched between pieces of aluminum foil and sealed in an aluminum can under a nitrogen environment. The DCS instrument was operated at an incident wavelength of 4.8 Å, corresponding to an energy resolution of 56.1 μeV and giving a time range of 2−50 ps. The spatial scale accessible by the DCS ranges from 0.55 to 2.13 $Å^{-1}$ (3−11 Å). The dynamic range of the HFBS instrument was ± 17 μeV, corresponding to an energy resolution of 0.85 μeV and giving a time range of 200−2000 ps. The accessible spatial range is 0.55 to 1.68 $Å^{-1}$ (4−11Å). Dynamic measurements were first made at 75 °C and then at 50 °C on both instruments, allowing 1 h for thermal equilibration at each temperature. A measurement was made at 22 °C using HFBS; however, PEO mobility was slower than the time scale of the instrument at this temperature. The neutron intensities were corrected with DAVE,[26] a data analysis software developed at NIST, for detector efficiency as compared with a vanadium standard, for scattering from an empty annular can, and for time-independent background scattering. The raw neutron intensity versus energy spectra ($S(q,\omega)$) were inverse-Fourier transformed to the time domain, where the instrument resolution was removed.[27]

Results and Discussion

Thermal Analysis and Ionic Conductivity Measurements. To characterize the bulk properties of our system, we measure the melting point, glass-transition temperature (T_g), extent of crystallization, and ionic conductivity. The DSC traces for each SPE are given in Figure 2. The samples are stored in a vacuum oven at 100 °C prior to the measurement, and the only crystalline phases expected under these heat treatment conditions are pure crystalline PEO and $(PEO)_3$:$LiClO_4$. During the scan, each sample was heated from room temperature to 200 °C, cooled to −90 °C, and reheated to 200 °C. The T_g of each sample is indicated in the Figure, along with the crystalline fraction of pure PEO (X_c). Data from the first and second heating are similar, indicating that pure PEO and $(PEO)_3$:$LiClO_4$ recrystallize within the time scale of the DSC measurement.

In the absence of $LiClO_4$, 78% of the pure PEO sample crystallizes at ∼60 °C. The crystalline fraction represents the fraction of the sample occupied by crystalline lamellae. The addition of $LiClO_4$ decreases the fraction of crystalline lamellae and depresses the melting point until the eutectic point is reached at 10:1 and 50 °C. Because a sufficient amount of time has not passed to observe the formation of the $(PEO)_6$:$LiClO_4$ phase, the 8:1 sample remains amorphous. When the lithium concentration is increased to 4:1, a melting endotherm is detected at ∼160 °C. A feature at this temperature is consistent with the presence of the $(PEO)_3$:$LiClO_4$ crystalline complex, as established by X-ray diffraction data.[1] However, the crystalline fraction of $(PEO)_3$:$LiClO_4$ cannot be calculated because the perfect heat of fusion for this phase is unknown.

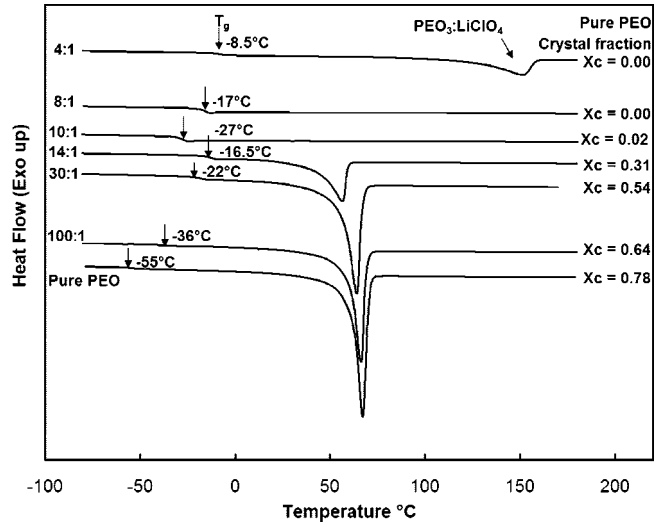

Figure 2. DSC traces as a function of $LiClO_4$ concentration. The T_g is marked with an arrow and the T_g values are given next to the arrow. The crystalline fraction of pure PEO is also included (X_c) at each $LiClO_4$ concentration.

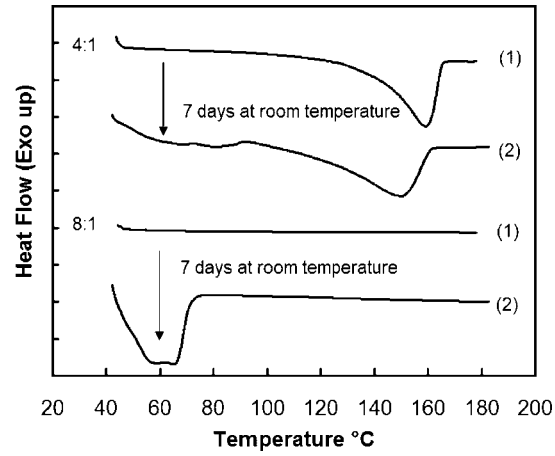

Figure 3. DSC traces for the 4:1 and 8:1 concentrations thermally treated two ways: (1) heated to 100 °C prior to the measurement (2) heated to 100 °C and stored at room temperature in a vacuum oven for 1 week prior to the measurement.

As mentioned above, the $(PEO)_6$:$LiClO_4$ crystalline phase can form if sufficient time has passed for crystallization. Figure 3 illustrates this point by comparing DSC data from two samples where the samples were (1) stored in a vacuum oven at 100 °C prior to the measurement and (2) heated to 100 °C and then stored in a vacuum oven at room temperature for 1 week. In case 2, sufficient time has passed for the formation of the $(PEO)_6$:$LiClO_4$ phase. In fact, a feature begins to emerge after just 3 days at room temperature. X-ray diffraction data for the 4:1 system indicates that pure PEO lamellae will not form; therefore, the feature near 60 °C that develops during 1 week is due to the formation of the $(PEO)_6$:$LiClO_4$ complex. Also, notice that the peak associated with the $(PEO)_3$:$LiClO_4$ crystal structure becomes broader when the sample is held at room

Table 3. Comparing the Overall to the Effective Coordination When Considering the Crystallization of Pure PEO[a]

overall EO:Li	X_c (%)	T_g (°C)	effective EO:Li
8:1	0	−17	8:1
10:1	2	−28	10:1
14:1	31	−16.5	8:1

[a] The T_g values reported in the table represent the midpoint of the T_g feature measured by DSC.

temperature for 1 week. This could indicate a broadening of the $(PEO)_3$:$LiClO_4$ crystal thickness distribution as a function of time.

The fraction of crystalline PEO is a function of lithium concentration and so is the T_g. In general, the T_g increases with increasing lithium concentration, indicating decreased polymer mobility; however, an exception occurs at a concentration of 10:1 (Figure 2). This can be explained by considering the extent to which pure PEO crystallizes in each sample and how much it increases the $LiClO_4$ concentration in the amorphous phase. Because the T_g is a measure of mobility in the amorphous regions, the T_g increases from the presence of additional lithium ions coordinating with ether oxygen atoms. We consider the fraction of the sample that crystallizes and calculate the new $LiClO_4$ concentration in the amorphous domains, labeled "effective concentration" in Table 3. We discover that the 14:1 sample has an effective concentration of ~8:1. Because the 10:1 sample is only 2% crystalline, the amorphous concentration remains ~10:1. On the basis of this, we expect the 8:1 and 14:1 samples to have similar T_g values and the 10:1 sample to have a lower T_g, which is consistent with the results illustrated in Figure 2.

Lastly, we measure the ionic conductivity of each sample as a function of temperature ranging from room temperature to 100 °C. Data are collected during a heat/cool/heat cycle. The data are illustrated by dividing the samples into two groups: samples where pure PEO does not crystallize to an appreciable extent (Figure 4A) and samples where pure PEO crystallizes to fractions varying from 31% (14:1) to 64% (100:1) (Figure 4B). The influence of crystallization on conductivity can be seen by the sharp decrease in conductivity near the melting point of pure PEO. Notice that even though the 14:1 sample is 31% crystalline, the effect of crystallization on conductivity is less severe than that for the 30:1 and 100:1 samples. In fact, the conductivity dependence on temperature for the 14:1 sample is similar to that for the 10:1 and 8:1 samples.

We also measured the conductivity at a concentration of 8:1 after the sample was held at room temperature long enough for the $(PEO)_6$:$LiClO_4$ crystalline complex to form. The result is illustrated in Figure 5, where the presence of the $(PEO)_6$:$LiClO_4$ complex decreases the conductivity by more than two orders of magnitude at room temperature. The sample was cooled and heated a second time with no indication of recrystallization. This complex has been shown to form lamellae in a similar system (PEO/LiTFSI), through which ionic conductivity was severely decreased. Whereas Li^+ transport may occur through this phase, the morphology of the lamellae prevents the long-range Li^+ transport that is required for high conductivity. As discussed above, transport through a crystalline phase does not guarantee high conductivity values; rather, proper orientation of the crystalline structures is also required.[18]

A compilation of bulk measurements are illustrated in Figure 6. Conductivity values are plotted at 22, 50, and 75 °C. Conductivity is maximized at 75 °C in the 14:1 sample, even though this sample contains fewer charge carriers than the 4:1, 8:1, and 10:1 samples. This implies that a balance must be achieved such that a sufficient number of Li^+ ions are available to conduct but not occupy all of the ether oxygens so that PEO mobility is significantly reduced. Our QENS measurements help us understand if this is the case, providing a link between PEO mobility and Li^+ ion mobility as a function of $LiClO_4$ concentration.

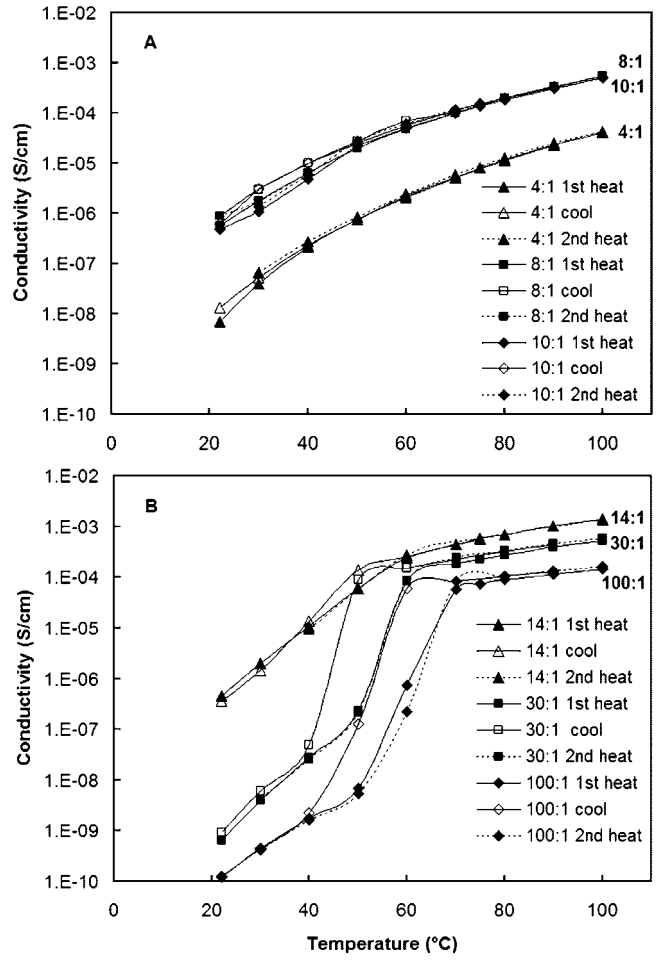

Figure 4. Conductivity as a function of temperature and $LiClO_4$ concentration for samples where pure PEO (A) does not crystallize and (B) crystallizes. The error in the data is on the order of the symbol size.

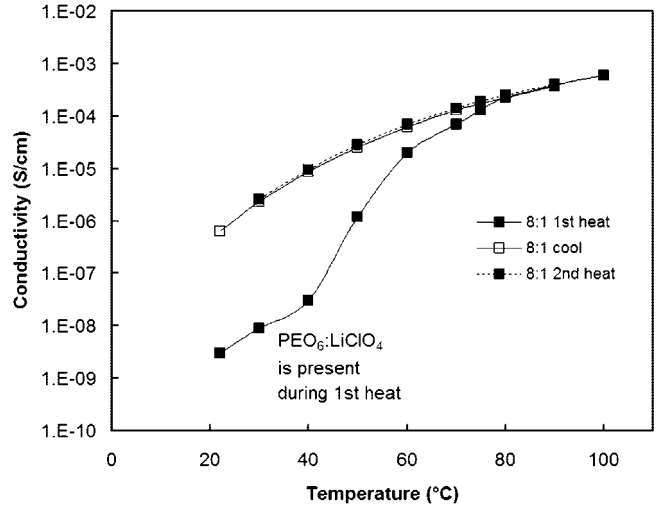

Figure 5. Conductivity as a function of temperature for the 8:1 sample where the $(PEO)_6$:$LiClO_4$ phase was allowed to form.

It is interesting to note that between 10:1 and 14:1, the T_g increases by more than 10 °C and the fraction of pure crystalline PEO increases from 2 to 31%, yet the conductivity also increases. Because the conductivity can be maintained even in

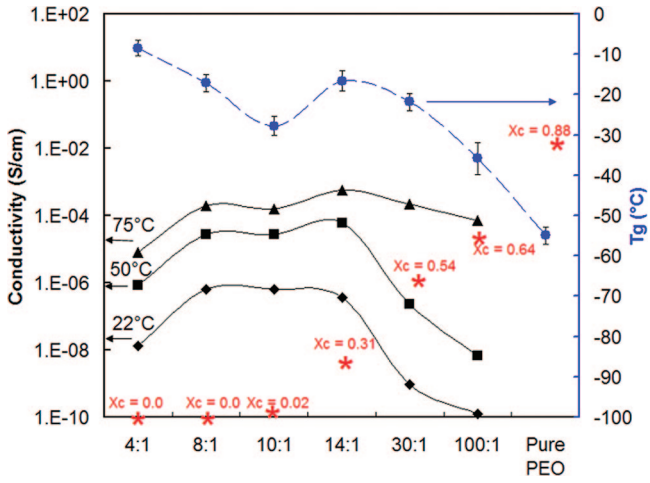

Figure 6. T_g (●), conductivity (75 (▲), 50 (■), and 22 °C (◆)), and pure PEO crystalline fraction (*) as a function of $LiClO_4$ concentration. The maximum and minimum T_g values represent the temperatures at which the T_g begins and ends on the DSC trace in Figure 2.

the presence of a significant fraction of crystalline PEO, we would like to understand the morphology of the crystalline phase. This includes the $(PEO)_3$:$LiClO_4$ complex present in the 4:1 sample. Even though conductivity can occur through crystalline structures, the larger morphology of the structure is also important.

Solid Polymer Electrolyte Structure Measured Using Small-Angle Neutron Scattering. SANS data as a function of temperature and lithium concentration are illustrated in Figure 7. The data are shifted along the *y* axis for clarity, with the shift factors given next to the data. There are three main features in the data that we will outline here and discuss in detail below. First, the sample with a concentration of 4:1 has a feature indicative of a cylinder at all temperatures: a change in slope from −4 at large *q* to a slope of −1 at small *q*. We expect the $(PEO)_3$:$LiClO_4$ crystalline complex to be present at this lithium concentration and at all temperatures measured; therefore, the cylindrical feature must be associated with this phase. Second, at 22 °C, concentrations ranging from 8:1 to pure PEO have a feature at $q \approx 0.01$ Å^{-1} that is most pronounced at intermediate $LiClO_4$ concentrations. The feature is also present at 50 °C in the concentration range of 14:1 to pure PEO and is completely absent for all concentrations at 80 °C. The temperature dependence of the feature is consistent with what we expect at these lithium concentrations and temperatures: pure crystalline PEO. Whereas the fraction of crystalline PEO decreases with $LiClO_4$, the contrast between crystalline PEO and amorphous PEO/$LiClO_4$ increases because of the presence of more $LiClO_4$. Higher contrast causes the crystalline feature to be more pronounced, even though the crystalline fraction is lower. The last feature appears in all of the data: a low *q* upturn with a slope of −4. Because the feature appears in pure PEO, it cannot be attributed to structures involving $LiClO_4$, and because it persists above the melting point of pure PEO, it cannot be attributed to PEO crystallization.

We begin with a discussion of the low *q* upturn feature because it appears in all of the data. A *q*-dependent intensity with slope of −4 indicates spheres and would also indicate long cylinders if the slope flattens to −1 at low *q* values outside the range of the instrument. Initially, we attributed the feature to voids in the sample caused by air bubbles. To test for this, we heated the sample to 100 °C under vacuum to decrease the number of voids. The SANS data under both conditions were identical, eliminating voids as a possibility. Although it is not possible to know the exact source of the feature, we estimated

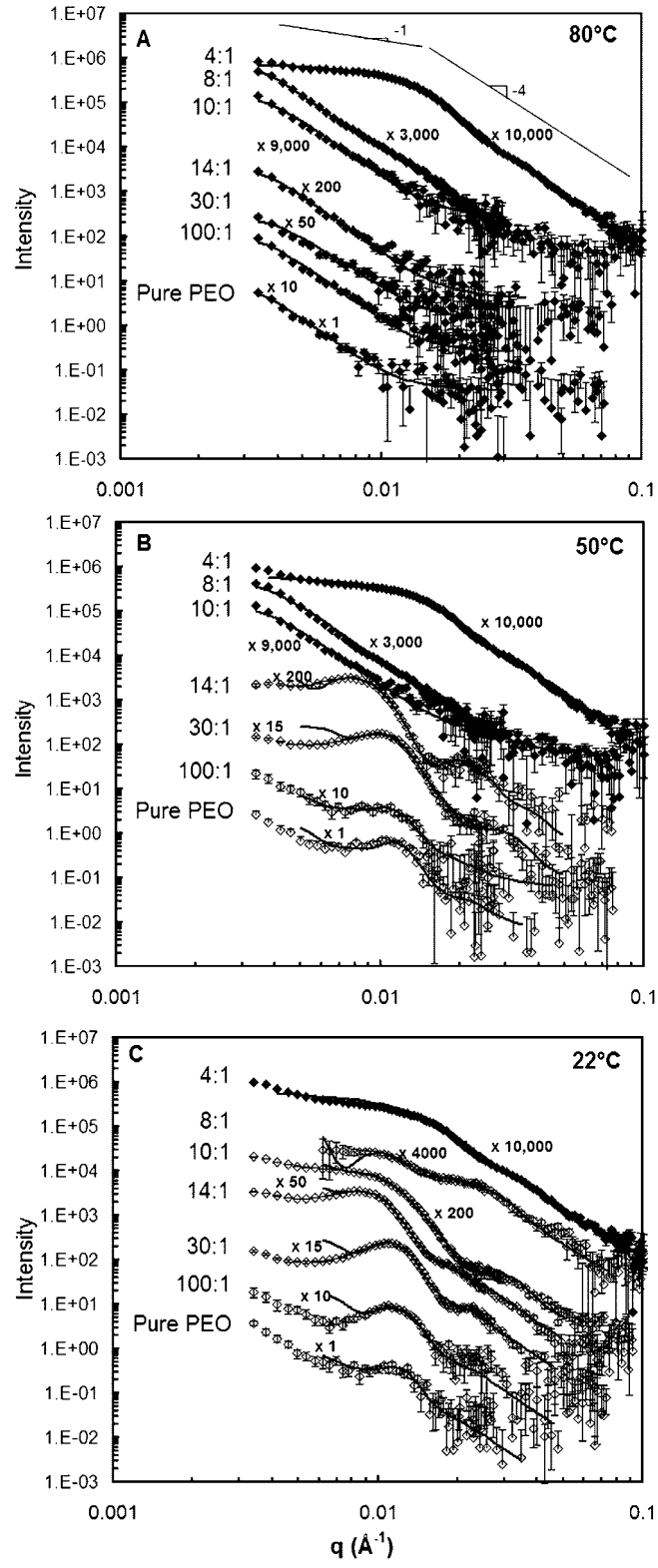

Figure 7. SANS data for all $LiClO_4$ concentrations and all temperatures: (A) 80, (B) 50, and (C) 22 °C. The data are shifted along the *y* axis from the original values for clarity, and the shift factor is given next to each data set. Unfilled symbols represent data for which the 80 °C data have been subtracted.

the size scale by fitting it to a polydisperse hard sphere model. The size estimated by the model could also correspond to the diameter of a long cylinder. Whatever the feature, we can estimate the smallest length scale that can describe the data. The polydisperse hard sphere model is given in ref 28. The fitting parameters include the radius, polydispersity, volume

fraction, and contrast. The smallest sphere that will fit the data is given by the q value where the intensity starts to increase for each sample ($q \approx 0.015$ Å^{-1}).

We test three hypotheses for the origin of the feature: crystalline nuclei, clusters of $LiClO_4$, and water clusters. The likelihood of crystalline nuclei is low on the basis of the fact that pure PEO has a well-defined melting point at 60 °C, and the DSC scans for all samples show no indication of crystallinity near 80 °C. However, considering the length scales measured by SANS, it seems reasonable that a small volume fraction of crystalline nuclei may exist that is not detectable by DSC. To test for this, we assume that the nuclei are pure PEO and set the contrast equal to the scattering length density difference between crystalline PEO and amorphous PEO, or in the case of lithium-containing SPEs, the difference between crystalline PEO and amorphous PEO/$LiClO_4$. The fit returns a volume fraction of ~0.04 for pure PEO. However, when $LiClO_4$ is added, and the contrast adjusted, the data cannot be fit with a physically meaningful volume fraction (~1.7). This unphysical result combined with DSC data that does not support crystallinity at 80 °C leads us to eliminate the possibility of crystalline nuclei as the reason for the low q upturn.

Next, we test the possibility that the slope arises because of clusters of pure $LiClO_4$. The flaw in this hypothesis is that it cannot be used to explain the pure PEO data. The contrast is set as the scattering length density difference between pure $LiClO_4$ and amorphous PEO/$LiClO_4$. This hypothesis is rejected because both the size and the volume fraction of the $LiClO_4$ clusters decrease with increasing $LiClO_4$ concentration (an unphysical result).

The final hypothesis we test is whether the feature could arise from water clusters. PEO is hydrophillic, and even though precautions were taken to keep the samples dry, it remains inevitable that some fraction of water was absorbed by the samples that a vacuum oven was unable to remove. In the case of pure PEO, we set the contrast as the difference between the scattering length densities of amorphous PEO and water. The smallest water cluster that fits the data has a diameter of 700 Å and a volume fraction of 0.0001. For samples that contain $LiClO_4$, we assume that the clusters are a mixture of water and $LiClO_4$. Neutron diffraction measurements of solutions of dPEO, D_2O, and LiI show that the ether oxygens of PEO do not compete with the D_2O for solvation of the Li^+ ion.[29] This demonstrates that when water is present, Li^+ ions will prefer to coordinate with water rather than with PEO ether oxygens. Because the oxygen in water is attracted to the Li^+ cation and the hydrogens with the ClO_4^- anion,[30] we assume two water molecules for every molecule of $LiClO_4$. By setting the contrast as the scattering length density difference between amorphous PEO/$LiClO_4$ and water/$LiClO_4$, we find that the smallest possible water/$LiClO_4$ clusters that fit the 100:1 to 8:1 data have a 400 ± 100 Å diameter present in volume fractions ranging from 0.0001 to 0.0003.

Thermogravimetric analysis (TGA) was used to ensure that water was not present in concentrations larger than that detected by SANS. We used TGA to monitor the mass of pure PEO while it was held at 80 °C under conditions similar to those of the SANS experiment. The temperature was then increased to 105 °C in an attempt to drive off water. The average value of the mass did not change within 30 min and fluctuated within 0.008 wt % of the average value. Considering the amount of water detected by SANS is ~0.01 wt % for pure PEO, a change in mass of this size cannot be detected within the accuracy of the instrument. Although this does not prove that water is responsible for the low q upturn, it shows that the volume fractions returned by SANS are not unreasonable if water is the source of the feature.

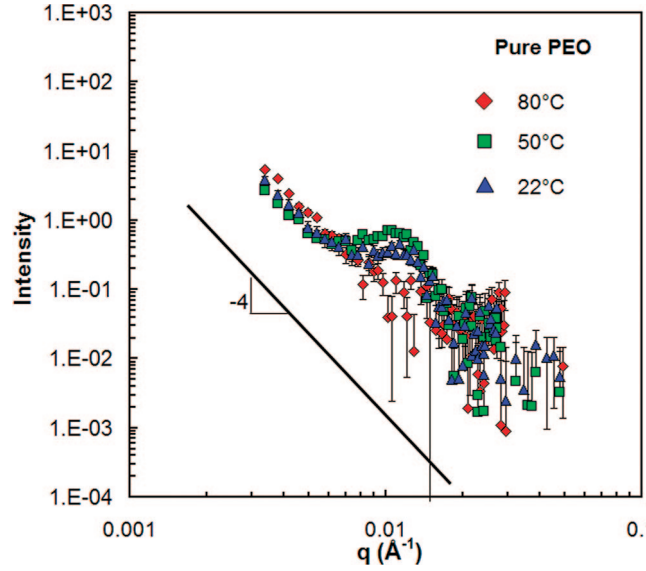

Figure 8. Pure PEO SANS data at 80, 50, and 22 °C. The feature indicated by the −4 slope in the data at 80 °C is also present 50 and 22 °C.

The upturn at 80 °C is similar in magnitude and slope at 50 and 22 °C for all samples. An example of this is illustrated in Figure 8 for pure PEO where the data are not shifted on the y axis. We assume that this small amount of water is temperature independent and present in all samples. Because we desire to isolate only the features that contribute to crystallization, we subtract the 80 °C data from the 22 and 50 °C data for the samples where pure PEO crystallizes. Pure crystalline PEO is indicated by a feature at $q \approx 0.01$ Å^{-1} for all data at temperatures below 80 °C with the exception of the 4:1 concentration, as well as 8:1 and 10:1 at 50 °C. This is consistent with our DSC results and with the PEO/$LiClO_4$ phase diagram.[1]

The data for which the 80 °C data have been subtracted are represented by open symbols in Figure 7. We fit this data using a model to describe concentrated lamellae that was developed in ref 31. The fitting parameters include the crystalline fraction, the lamellar spacing (long period), the bilayer thickness, the polydispersity of the bilayer thickness, the contrast, the number of repeating lamellar plates, and the Caille parameter. The Caille parameter accounts for thermal fluctuations along the crystalline and amorphous interface, causing the interface to be less well defined. A value approaching one represents a poorly defined interface. We assume that the crystalline regions are pure PEO so the contrast is set as the scattering length density difference between pure crystalline PEO and amorphous PEO/$LiClO_4$. We account for the $LiClO_4$ concentration increase in the amorphous domains due to the $LiClO_4$ that is expelled from the crystalline domains. The fit lines are illustrated in Figure 7. The model overestimates the data that a low q due to powder averaging included in the model, and it is therefore more important to fit the Bragg peaks at $q \approx 0.01$ Å^{-1} and $q \approx 0.02$ to 0.03 Å^{-1}.[25] Fits to the data return a lamellar spacing for pure PEO of ~500 Å, which is in agreement with small-angle X-ray scattering measurements of 470 Å.[32] The lamellar spacing is the sum of the lamellar thickness plus the thickness of the amorphous region between lamellae. The crystalline fraction and lamellar spacing are given in Figures 9 and 10 as a function of temperature. As depicted by the cartoons in Figure 10, the thickness of the crystalline lamellae is comparable to the thickness of the amorphous domain between the lamellae (bilayer thickness) for samples that contain $LiClO_4$. All fit parameters returned from the lamellar model are provided in Table 4.

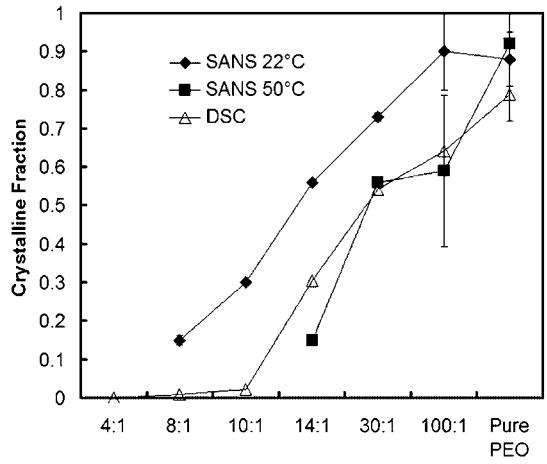

Figure 9. Pure PEO crystalline fraction from DSC and SANS at 22 and 50 °C as a function of $LiClO_4$ concentration.

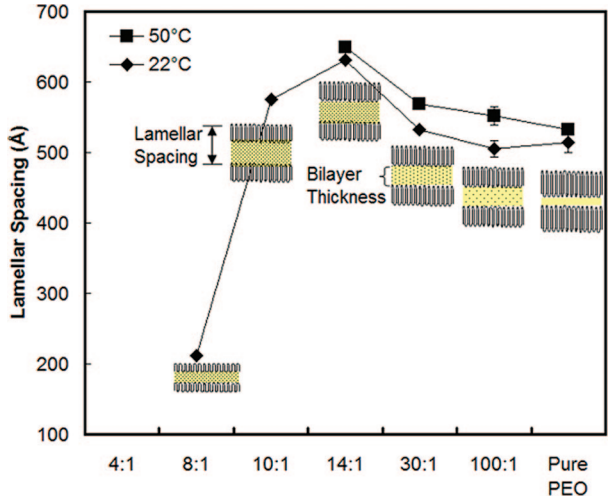

Figure 10. Lamellar spacing as a function of $LiClO_4$ concentration and temperature.

The crystalline fraction detected by SANS is larger than that from DSC for all samples. This is due to the fact that the SANS crystalline fraction represents the fraction of the sample that can be fit with the lamellar model (this includes crystalline lamellae and the amorphous material between lamellae), whereas the DSC fraction represents only the fraction of crystalline lamellae in the entire sample. If we consider the ratio of crystalline lamellae to the amorphous material between lamellae (Table 4) and multiple this by the SANS crystalline fraction, then the values are close to those measured by DSC. In addition, the crystalline fractions returned by SANS for all samples at 22 °C are consistent with a 6:1 ratio in the amorphous domains between crystalline lamellae. This suggests that pure PEO has fully crystallized in all samples, and any further crystallization would involve the $(PEO)_6$:$LiClO_4$ crystalline complex.

Figure 10 indicates that the sample with the largest lamellar spacing has a concentration of 14:1. This is the same sample that shows the highest conductivity at 50 °C despite containing a significant amount of pure crystalline PEO. This result suggests that perhaps crystallization has more of an influence on the SPE than simply increasing the $LiClO_4$ concentration in the amorphous domain. This is supported by the fact that the 8:1 and 14:1 samples have the same effective $LiClO_4$ concentration (8:1), and yet the sample with the crystalline fraction of 31% has the higher conductivity value. Perhaps the crystalline lamellae in the 14:1 sample create regions of confined, amorphous PEO/$LiClO_4$ where the polymer dynamics are affected and Li^+ transport is increased. Or perhaps the crystalline interface creates a directed pathway for Li^+ transport. In both cases Li^+ transport would be directed but short-ranged. As mentioned above, the macroscopic structure of the SPE must accommodate Li^+ transport from one electrode to the other for battery operation.

Lastly, we consider the cylindrical features present in the 4:1 sample at all temperatures. The data can be fit to a flexible cylinder model with a polydisperse radius. The details of the model are given in ref 33 with corrections in ref 34. The fitting parameters include the fraction of cylinders, the contour length of the cylinder, the Kuhn length (flexible segment length), the radius, the radius polydispersity, and the contrast. We set the contrast to be the scattering length density difference between $(PEO)_3$:$LiClO_4$ and amorphous PEO/$LiClO_4$. The radius of the crystalline cylinders is ~125 Å with a length of ~700 Å. The volume fraction occupied by the cylinders is ~0.16 and does not change with temperature. All fitting parameters returned by the cylindrical model are reported in Table 5.

As mentioned above, the $(PEO)_3$:$LiClO_4$ phase is present at this composition at all measured temperatures. Although the structure of the $(PEO)_3$:$LiClO_4$ complex is unknown, the structures of similar complexes have been resolved. In the case of $(PEO)_3$:X, where X is $NaClO_4$,[35] NaI,[36] $LiCF_3SO_3$,[37] and LiTFSI,[19] a cation (Li^+ or Na^+) is located inside each turn of a PEO helix and is coordinated with three ether oxygen atoms on the PEO chain. This is different than the 6:1 crystalline complex that requires six ether oxygens from two PEO chains. Unlike the 6:1 complex, the 3:1 complex requires additional coordination from two anions located outside the PEO helix.[14] Given the similarity between these SPEs and PEO/$LiClO_4$, it seems reasonable that $(PEO)_3$:$LiClO_4$ would have a similar tunnel-like structure. Whereas the average width of the crystalline complex cannot be resolved with SANS (for example, the diameter of the $(PEO)_3$:$LiCF_3SO_3$ complex is ~10 Å,[37]), multiple tunnels aligned side-by-side could be detected via SANS. Our data are consistent with this picture: the alignment of cylinders of $(PEO)_3$:$LiClO_4$ with radius 125 Å. The alignment could result from the additional coordination required by the 3:1 complex that is not required in the 6:1 complex. The diameter of the cylinders corresponds to the length of the crystalline lamellae (200−300 Å) in the concentration range of 8:1 to 100:1. We calculated this length by subtracting the bilayer thickness from the lamellar spacing returned by the fitting procedure. This suggests the possibility of a fundamental length scale over which the crystalline structures are able to form between amorphous domains, regardless of the identity of the crystalline complex. In this case, the contour of the $(PEO)_3$:$LiClO_4$ cylinders could consist of crystalline segments alternating with amorphous segments, which accounts for the flexible nature of the cylinder.

At 22 °C, an additional contribution must be included to accurately fit the 4:1 data. In this case, we combine the contribution from the flexible cylinder model with a small contribution from crystalline lamellae. Because pure PEO does not crystallize at this $LiClO_4$ concentration, the crystalline lamellae are from the $(PEO)_6$:$LiClO_4$ complex. In this case, instead of using the scattering length density of pure PEO to calculate the contrast, we use the scattering length density of $(PEO)_6$:$LiClO_4$. The contrast is calculated as the difference between $(PEO)_6$:$LiClO_4$ and amorphous PEO/$LiClO_4$ while accounting for the fraction of lithium that is involved in the $(PEO)_3$:$LiClO_4$ phase. The volume fraction of $(PEO)_6$:$LiClO_4$ is 0.06 in the 4:1 sample at 22 °C, and the lamellar spacing is 180 Å. Although this small contribution is required to fit the data at 22 °C, the DSC scan illustrated in Figure 2 does not

Table 4. Fit Parameters for Pure PEO Crystalline Lamellae[a]

concentration	crystal fraction	lamellar spacing (Å)	bilayer thickness (Å)	polydispersity	no. lamellar plates	Caille parameter
			22 °C			
8:1	0.15 ± 0.01	212 ± 0.95	91 ± 7	0.70 ± 0.10	4 ± 0.0	1.0 ± 0.0
10:1	0.30 ± 0.01	575 ± 1.3	287 ± 1	0.15 ± (2 × 10^{-3})	4 ± 0.0	1.0 ± (9 × 10^{-4})
14:1	0.56 ± 0.01	631 ± 1.6	342 ± 2	0.25 ± (4 × 10^{-3})	4 ± 0.2	0.54 ± 0.01
30:1	0.73 ± 0.01	532 ± 0.77	206 ± 3	0.53 ± 0.02	4 ± 0.0	0.32 ± (4 × 10^{-3})
100:1	0.9 ± 0.10	505 ± 11	200 ± 20	1 ± 0.81	4 ± 3.0	0.42 ± 0.13
pure PEO	0.88 ± 0.10	514 ± 14			82 ± 28	0.53 ± 0.13
			50 °C			
14:1	0.15 ± (4 × 10^{-3})	650 ± 6	412 ± 4	0.13 ± 0.01	4 ± 0.13	0.41 ± 0.06
30:1	0.56 ± (5 × 10^{-3})	569 ± 1.4	293 ± 2	0.15 ± 0.01	4 ± 0.1	0.49 ± 0.03
100:1	0.59 ± 0.2	552 ± 13	193 ± 84	0.76 ± 0.80	5 ± 5	0.54 ± 0.24
pure PEO	0.92 ± 0.2	532 ± 8			5 ± 3	0.3 ± 0.13

[a] The polydispersity represents the polydispersity of the bilayer thickness. Blank entries indicate parameters that could not be resolved by the model.

Table 5. Fit Parameters for Cylindrical Features in the 4:1 Sample[a]

concentration, T (°C)	crystal fraction	contour length (Å)	radius (Å)	polydispersity	Kuhn length (Å)
4:1, 22	0.16 ± 0.05	606 ± 8	121 ± 2	0.22 ± 0.02	10 ± 2.4
4:1, 50	0.16 ± 0.05	677 ± 2	124 ± 0.2	0.24 ± (2 × 10^{-3})	4 ± 0.17
4:1, 80	0.16 ± 0.05	770 ± 2	134 ± 0.2	0.20 ± (1 × 10^{-3})	9 ± 0.15

[a] The polydispersity represents the polydispersity of the radius.

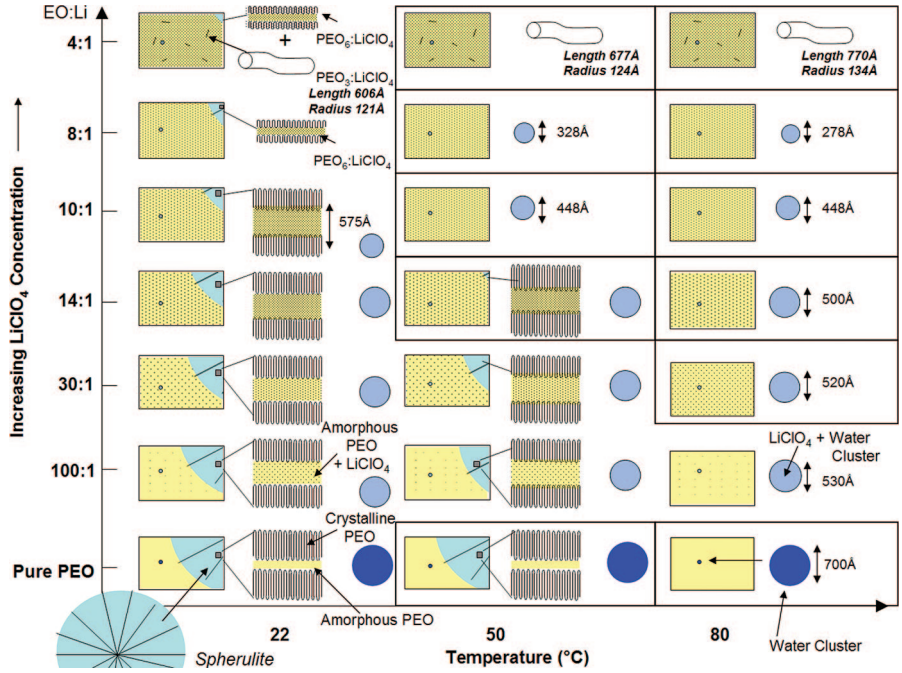

Figure 11. Summary of SANS results at all temperatures and $LiClO_4$ concentrations. Boxes indicate samples measured using QENS.

indicate the presence of the $(PEO)_6$:$LiClO_4$ complex in the 4:1 sample. In fact, the DSC scan shown in Figure 3 illustrates that it requires days at room temperature for this complex to form to an extent detectable by DSC. We conclude that within minutes or hours after heating above 100 °C, the $(PEO)_6$:$LiClO_4$ phase forms to an extent that is detectable by SANS but not DSC.

A summary of the SANS results is given in Figure 11, where the structure of each sample is depicted by a cartoon. Each column represents a different temperature, and each rectangle represents a portion of the SPE. The small black dots inside the rectangle represent Li^+ and ClO_4^- ions. The Figure illustrates how the volume fraction of pure PEO lamellae decreases with increasing temperature and $LiClO_4$ concentration. Notice that the $(PEO)_3$:$LiClO_4$ crystalline structure does not change with temperature in the 4:1 sample, which is consistent with the diffraction results as a function of temperature at this concentration. The blue circles designate the water or water/$LiClO_4$ clusters that are present in all samples.

PEO Mobility Measured Using Quasi-Elastic Neutron Scattering. QENS is used to measure PEO mobility at the following $LiClO_4$ concentrations and temperatures: 4:1, 8:1, 10:1, 14:1 and pure PEO at 50 and 75 °C as well as 30:1 at 75 °C. By combining the structural information from SANS, conductivity data, and a direct measure of PEO mobility, we can evaluate the role of PEO mobility in semicrystalline SPEs. The 4:1 sample is semicrystalline at both temperatures, where the crystalline complex is $(PEO)_3$:$LiClO_4$. As we learned from SANS, bundles of these crystalline complexes form cylinders that are approximately 700 Å long with a radius of ~125 Å. The remaining samples are fully amorphous at 75 °C. When the temperature is lowered to 50 °C, the 14:1 and pure PEO samples crystallize. The crystalline phase that forms is pure PEO because we do not wait long enough for the $(PEO)_6$:$LiClO_4$ phase to form. The 8:1 sample remains amorphous at 50 °C because pure PEO does not crystallize at this concentration. Also, the 10:1 sample remains amorphous at 50 °C because

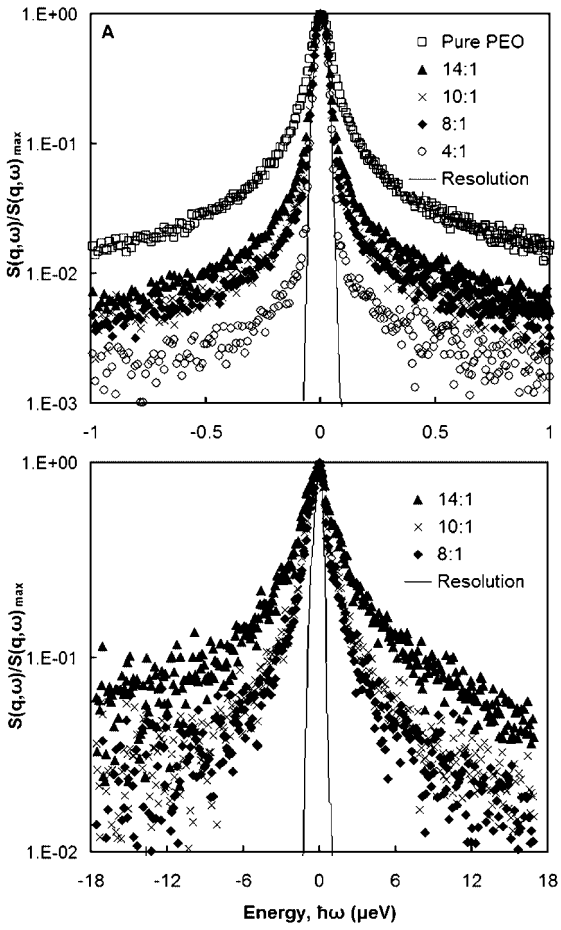

Figure 12. Incoherent structure factor in the frequency domain for several samples measured using (A) DCS and (B) HFBS at 75 °C and $q = 1.04$ Å^{-1}.

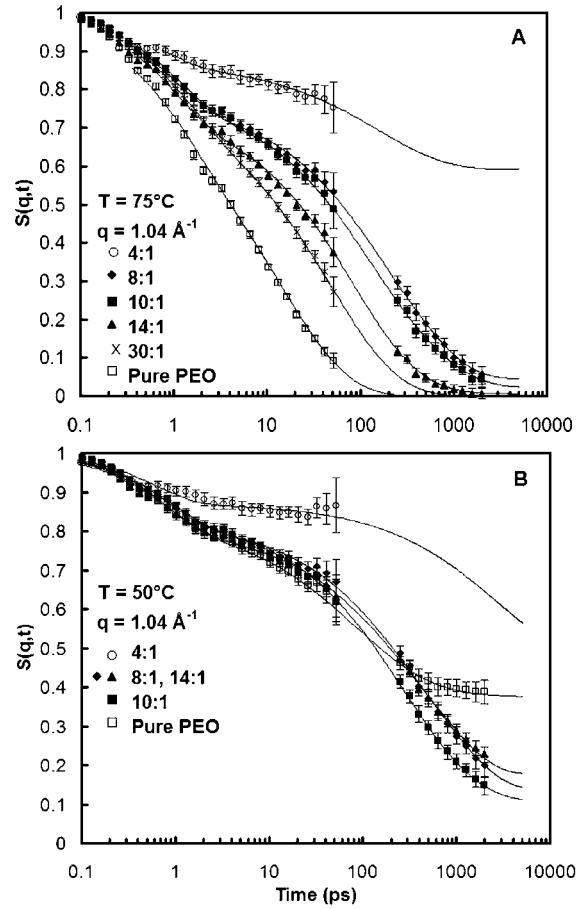

Figure 13. Self-intermediate scattering function at (A) 75 and (B) 50 °C for $q = 1.04$ Å^{-1}. The data at short time are from DCS and the data at longer time are from HFBS. The lines through the data are fits to the Kolraush−Williams−Watts (KWW) expression.

this temperature and concentration correspond to the eutectic point of PEO/$LiClO_4$. Although the crystalline phases present in the QENS samples are not expected to influence Li^+ mobility, we do expect them to influence PEO mobility.

QENS detects changes in energy and momenta of scattered neutrons, reflecting the time and space dependence of the mobility of atoms in the sample. The number of neutrons scattered as a function of energy and spatial scale is given by the incoherent structure factor, $S(q,\omega)$. These data are illustrated in Figure 12A,B in the frequency domain for selected samples at 75 °C and one spatial scale ($q = 1.04$ Å^{-1}). Figure 12A illustrates data from the DCS instrument, and Figure 12B illustrates data from the HFBS instrument, where $S(q,\omega)$ is convoluted with the instrument resolution. The connection between data from different instruments and the numerical treatment of the stretched exponential is better suited to the time domain. Therefore, we inverse Fourier transform the data before analysis to the self-intermediate scattering function, $S(q,t)$. All samples measured at 75 and 50 °C are illustrated in Figure 13A,B ($q = 1.04$ Å^{-1}). The DCS data include values less than ~40 ps, and the HFBS data include values greater than ~200 ps. As discussed below, the data are fit as received from the inverse Fourier transform. The HFBS data in Figure 13A,B are scaled to present the data on a continuous curve. The scaling accounts for the fact that the decay is measured in two pieces (a sum), whereas the decay can be split in this way only if it represents distinct processes that are well separated in time. This treatment is for display purposes only and does not influence the fitting procedure or the resulting fit parameters.

Before providing a detailed analysis of the data, we point out several general features. First, the mobility of PEO decreases with increasing $LiClO_4$ concentration in the amorphous state (75 °C). This is consistent with previous observations of PEO-based SPEs in the amorphous phase.[10,38] The slow mobility can be attributed to the coordination of ether oxygens with Li^+ ions.

Second, the 4:1 sample has a slower and different mobility than the others at both 75 and 50 °C. On timescales less than 1 ps, where cage vibrations are detected, the mobility of the 4:1 sample is slower than that of samples containing less lithium. This reflects stronger binding between Li^+ ions and PEO in the 4:1 sample.

Third, the influence of crystallinity on mobility is reflected in Figure 13B. According to the SANS data at 50 °C (Figure 9), pure PEO crystallizes 80%, 14:1 crystallizes 15%, and 10:1 and 8:1 are amorphous. The mobility in Figure 13B reflects the motion of amorphous regions slowed by attachment to crystalline regions or local coordinations with Li^+ ions. In both cases, the mobility is slowed by the same amount. As mentioned above, the 4:1 sample is significantly different, supporting the fact that its local coordination is more restrictive than the others. Perhaps physical cross-links exist between chains because of the high lithium concentration. The difference between the 4:1 sample and the others cannot be attributed to crystallization because the crystal fraction (0.17) is similar to that of 14:1 and much less than that of pure PEO.

Fourth, the 10:1 sample is the most mobile at 50 °C, whereas the 8:1 and 14:1 samples have similar mobilities. As discussed above, the effective concentration of $LiClO_4$ in the amorphous

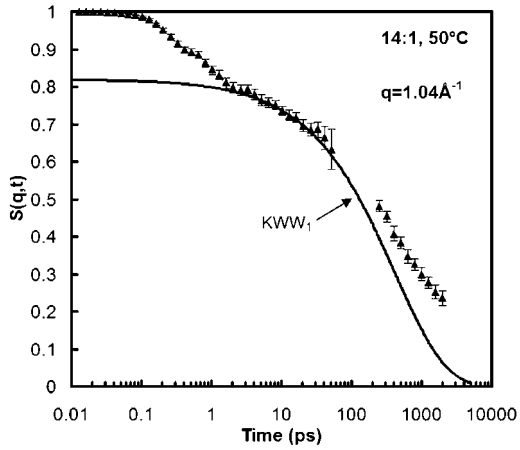

Figure 14. Attempted fit of DCS and HFBS data with one stretched exponential.

regions of a semicrystalline sample will be higher than the overall concentration. For the QENS measurements, this applies only to the 14:1 sample. As discussed above, the effective concentration of this sample increases from 14:1 to 8:1 at 22 °C. At 50 °C, the effective concentration increases from 14:1 to 10:1 because the 14:1 sample is less crystalline at this temperature than at 22 °C. Consequently, we would expect the mobility of the 14:1 and 10:1 samples to be equal; however, the 10:1 sample is more mobile at 50 °C. Despite its fast mobility, recall that the 10:1 sample does not have the highest conductivity at 50 °C (Figure 6). Instead, the less-mobile 14:1 sample has the highest conductivity despite the fact that it is partially crystalline at 50 °C. Because the 10:1 and 14:1 concentrations have equal effective $LiClO_4$ concentrations in the amorphous phase, we would also expect equal conductivities on the basis of the argument that conductivity and polymer mobility are strongly coupled. The fact that the conductivity at 14:1 is greater suggests a decoupling of polymer mobility from Li^+ mobility in the presence of crystallinity.

To quantify these observations and determine their dependence on a spatial scale, we fit the $S(q,t)$ data to a Kolraush−Williams−Watts (KWW) stretched-exponential equation

$$S(q,t) = \text{EISF} + (1 - \text{EISF}) \exp\left[-\left(\frac{t}{\tau(q,T)}\right)^{\beta(q,T)}\right] \quad (1)$$

The fitting parameters include the polymer relaxation time, τ, the distribution of relaxation times, β, and the elastic incoherent structure factor, EISF. This equation is generally applicable to describing relaxation behavior in polymers.

The initial decay that occurs on timescales of less than 2 ps has been observed for other polymers and is associated with cage vibrations and torsional librations. At times longer than 2 ps, the mobility captured by the DCS instrument is associated with the segmental motion of the polymer, and we will refer to this process as KWW_1. The DCS and the HFBS data cannot be fit to a single process, as illustrated in Figure 14 for the 14:1 sample at 50 °C and $q = 1.04$ Å^{-1}. As a result, we use more than one KWW expression to fit the data. The segmental portion of the DCS data is fit to KWW_1, and these parameters are held constant while the HFBS data are fitted. The HFBS is fit to the sum of two stretched exponentials, $KWW_1 + KWW_2$, and thus fitting parameters are assigned for only KWW_2. We determine that fits to KWW_1 are improved by including the initial decay associated with vibrations because this more accurately describes the region where the two processes are mixed.

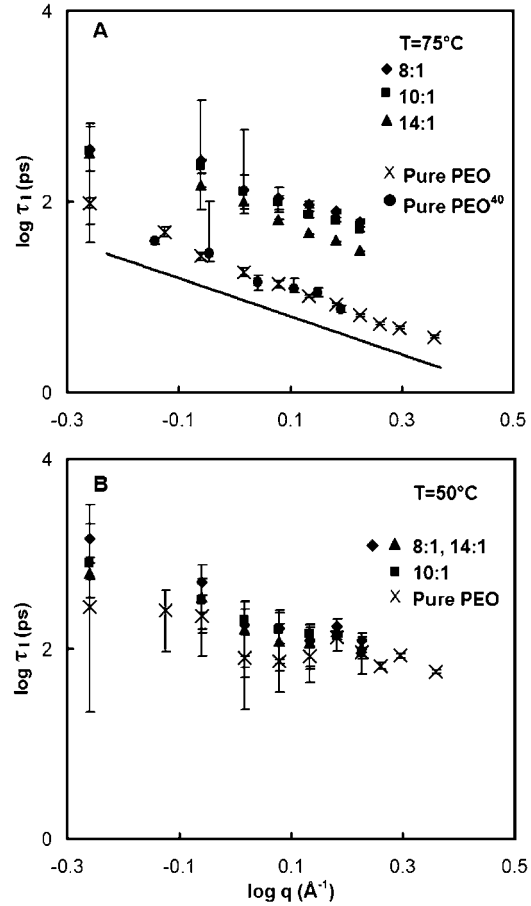

Figure 15. τ_1 as a function of q and $LiClO_4$ concentration at (A) 75 and (B) 50 °C. The error bars represent one standard deviation from the average. The closed circles at 75 °C represent data reported in ref 40 and the line represents $\tau \sim q^{-2}$. $\beta_1 = 0.6$ for all samples.

Considering the small time range measured by DCS, we fix β for the KWW_1 process at 0.6 because this is the expected value for the segmental relaxation of pure PEO based on previous measurements with a larger time range.[39] We do not fix β for the KWW_2 process because we are not sure of its origin. Error is assessed using a previously established procedure.[27] 500 data sets are generated on the basis of the original $S(q,t)$ data and associated error bars, and each data set is fit using different initial guesses for the fit parameters. We report the average value of the 500 fits along with error bars that represent one standard deviation from the average. The error bars represent the range of each parameter that can accurately fit the data within one standard deviation while leaving the other fitting parameters unconstrained. The fits to the data are presented as a product, $S(q,t) = KWW_1KWW_2$, in Figure 13. The fit lines are generated using the parameters obtained by fitting each data set, as described above.

The τ_1 values resulting from the fit of KWW_1 to the DCS data are illustrated in Figure 15A,B (75 and 50 °C, respectively) as a function of q. The pure PEO τ_1 values are consistent with previous QENS results for amorphous PEO.[40,41] The spatial dependence, $\tau \propto q^{-2/\beta}$, is characteristic of segmental motion in polymers and supports the fact that the KWW_1 process captured by DCS reflects the segmental relaxation of the PEO backbone. As expected, the segmental relaxation times increase as the concentration of $LiClO_4$ increases, and this is particularly strong at 75 °C, where no crystalline PEO is present. Although $LiClO_4$ slows the mobility of the polymer, it does not impact the type of motion because the spatial dependence of τ_1 continues to

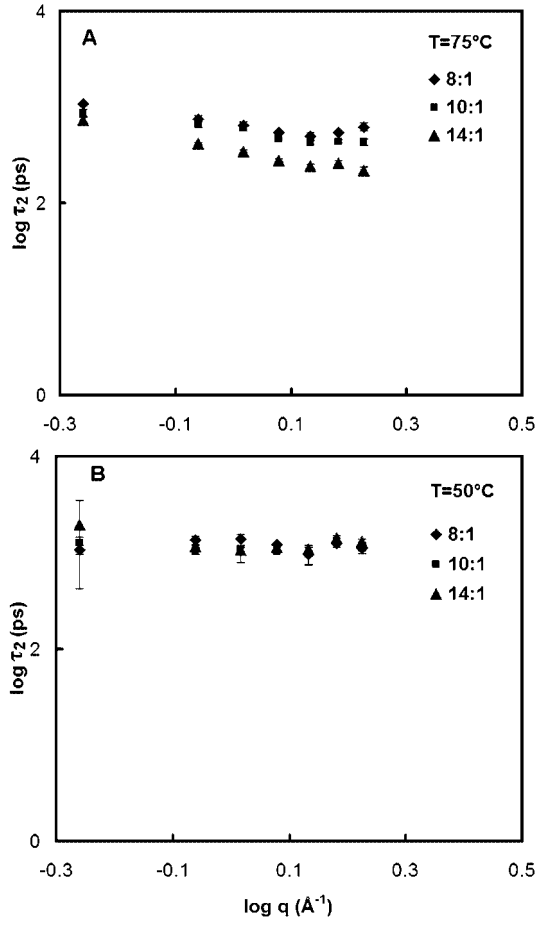

Figure 16. τ_2 values as a function of q and $LiClO_4$ concentration at (A) 75 and (B) 50 °C. The error bars represent one standard deviation from the average. The β_2 values range from 0.7 to 0.9 at 75 °C and 0.8 to 1.0 at 50 °C.

suggest segmental motion. This means that even though the backbone of the polymer is less mobile at the locations at which it is coordinated with Li^+ ions, the sections that are mobile retain translational character.

Unlike the first process, we are unsure of the origin of the second process and therefore do not constrain β for KWW_2. The fitting results indicate that β_2 covers a range of values varying from 0.7 to 0.9 at 75 °C and 0.8 to 1.0 at 50 °C. The relaxation times associated with the second process, τ_2, are illustrated in Figure 16A,B (75 and 50 °C, respectively) as a function of q. The relaxation times are independent of the spatial scale, which is a signature of a rotational process. Although a rotational process would not be observed in a polymer with no side groups such as pure PEO, the addition of Li^+ gives rise to structures that could potentially result in the rotation of protons. As discussed above, diffraction studies have revealed the formation of cylinders formed by PEO wrapping around Li^+ ions. These cylindrical structures persist to some extent in amorphous PEO/$LiClO_4$.[6] We test if the geometry of the motion we observe is consistent with the structures identified by diffraction. For example, the protons surrounding the Li^+ ion in the cylindrical structure may rotate on or within a circle, where the center of the circle is the axis of the cylinder.

To characterize the geometry of motion, we examine the spatial dependence of $EISF_2$, illustrated in Figure 17A,B at 75 and 50 °C, respectively. We begin with the 50 °C data because more crystallinity is present. We first consider protons jumping among discrete sites on a circle. This model does not accurately

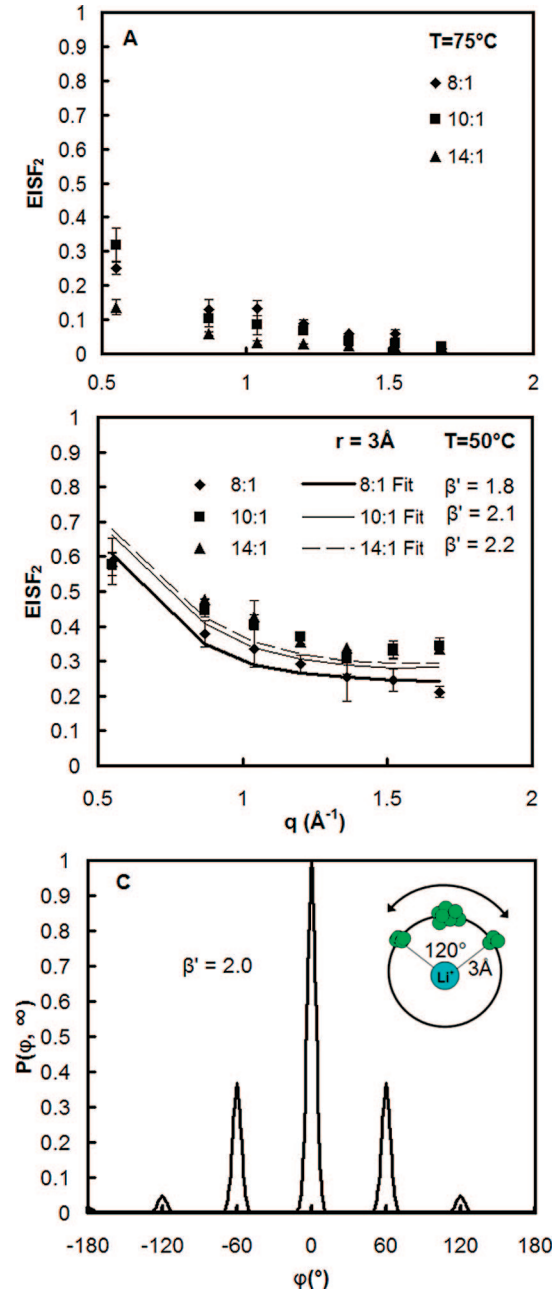

Figure 17. $EISF_2$ values as a function of q and $LiClO_4$ concentration at (A) 75 and (B) 50 °C. The error bars represent one standard deviation from the average. The fit lines in (B) are from the model describing uniaxial rotation with a nonuniform distribution (eq 2). The angular distribution is illustrated in (C) for $\beta' = 2.0$. The inset in C depicts the distribution, where the spheres indicate the location of hydrogen atoms on a circle with a radius of 3 Å.

represent the data, even when the number of jump sites is varied. The same is true for continuous rotation on a circle. If the motion we observe is the result of protons wrapping around and coordinating with Li^+ ions, then we would expect the proton rotation to be restricted because of connectivity with the PEO backbone and coordination with the Li^+ ions. Therefore, we test a model that describes rotation with a nonuniform distribution.[42] In this case, rotation occurs over a circle where the points on the circle are not equally weighted. As a result, the probability of a locating a proton at a particular angle on the circle is defined by a peaked distribution. This model represents our data, and the EISF as a function of q is given by

$$\mathrm{EISF}(q) = \frac{1}{NI_o^2}\sum_{n=1}^{N} j_o\left(2qr\sin\frac{\pi n}{N}\right) I_o\left(2\beta'\left|\cos\frac{\pi n}{N}\right|\right) \quad (2)$$

where r is the radius of the circle, N is the number of sites on the circle, $j_o(x)$ is a Bessel function of the first kind, $I_o(x)$ is a modified Bessel function of the first kind, and β' defines how strongly the angular distribution is peaked. The angular distribution at time $\rightarrow \infty$ is given by

$$P(\phi,\infty) = \frac{2\pi}{N}\sum_{n=1}^{N}\delta(\phi-\phi_n)\exp\left[\beta'\cos\left(\frac{2\pi n}{N}\right)\right] \quad (3)$$

where ϕ denotes the angular position on the circle and ϕ_n represents the angle of each site, n, on the circle. If β' equals zero, then there is no preferred angular orientation, and jumps among N equivalent sites on a circle are recovered (a model that does not describe our data). A reasonable fit can be achieved when we set the number of sites equal to six, the radius equal to ~3 Å, and β' equal to values ranging from 1.8 to 2.2 (Figure 17B). The distribution is illustrated in Figure 17C for $\beta' = 2.0$. The majority of the protons are restricted to rotating among three sites (120° of a circle with six sites). This type of motion is consistent with the rotation of PEO hydrogen atoms around the Li^+ ions in a cylinder. One piece of evidence that supports this picture is that the radius returned by our fit (~3 Å) corresponds to the Li−H distance in the cylinder measured by diffraction.[6]

Even though an EISF that describes rotation does not normally depend on temperature, the fraction of rotating protons decreases at 75 °C (Figure 17A) compared with that at 50 °C (Figure 17B). This data cannot be fit to a model that describes pure rotation (restricted or otherwise). The fact that τ_2 weakly depends on q at 75 °C, whereas it is independent of q at 50 °C, suggests that an additional type of motion is entering the window of the instrument at high temperature. Therefore, we cannot expect a model that describes only rotation to fit the data. It seems reasonable that the fraction of rotating cylinders that persist at high temperature would be smaller than that at low temperature. This is consistent with neutron diffraction data where the size of the peak associated with the cylindrical structures decreases when the sample is heated to 100 °C.[6] The size of the peak does not change upon subsequent cooling to room temperature, indicating that the fraction of cylinders depends on the thermal history of the sample.

We examine our results in the context of previous QENS studies. As mentioned in the introduction, either one or two processes have been observed using QENS, depending on the identity of the anion. One process was observed for amorphous PEO/LiI and PEO/$LiClO_4$, whereas two processes were observed for amorphous PEO/LiTFSI and PEO/LiBETI. In the case of PEO/$LiClO_4$, our QENS data extend to longer timescales, and we are able to capture a second process. In the case of PEO/LiI, the data fully decay in the window of the instrument and do not reveal a second process. The variable that differs in these systems is the Li^+ coordination (Table 1). For the samples containing $LiClO_4$, LiTFSI, and LiBETI where two processes were observed, the ether-oxygen-to-lithium coordination is 6:1 at the lithium concentrations measured by QENS. The intermediate-ranged structure includes two PEO chains wrapping around the Li^+ ions in a cylindrical structure. In contrast, the LiI sample is coordinated by three ether oxygens forming a tight PEO helix around the Li^+ ions, and it requires additional coordination from two anions located outside the helix. The cross-linking between the Li^+ ions and the anions could prevent proton rotation in the PEO helix, and this could be why a second process is not observed for PEO/LiI.

It is useful to examine the processes separately to identify how much each process is influenced by temperature and $LiClO_4$ concentration. As mentioned above, the $S(q,t)$ data plotted in Figure 13A,B represent the product of KWW_1 and KWW_2 because the two processes overlap. To examine them individually, we plot KWW_1 and KWW_2 at 50 and 75 °C for $q = 1.04$ $Å^{-1}$ in Figure 18A−D. The fits illustrate the fact that the segmental process, KWW_1, is more strongly coupled to the $LiClO_4$ concentration than the rotational process, KWW_2. In fact, at 50 °C, the rotational process is independent of $LiClO_4$ concentration. This suggests that rotation likely has little to do with the conductivity, and instead, the first process describing segmental motion should be considered in the context of conductivity. We directly compare the conductivity values with the relaxation times for the first process as a function of lithium concentration by plotting them in Figure 19. Recall that our fitting procedure generates 500 sets of fitting parameters, and because the parameters are not constrained, a large range of values is returned. To compare the τ_1 values at each lithium concentration directly, we extract the set of fitting parameters for which the $EISF_1$ values are equal; in this case, we choose $EISF_1 = 0.1$. The τ_1 from this set of parameters is illustrated in Figure 19. At 75 °C, the relaxation times and conductivity values have a similar dependence on lithium concentration in the range of 4:1 to 14:1. At lower lithium concentrations, mobility increases because of less ether oxygen/Li^+ cross-links, whereas conductivity decreases because of the reduced number of charge carriers. If we were to predict what sample would have that maximum conductivity at 50 °C on the basis of the data at 75 °C, we would choose the 10:1 sample. Not only does it have more charge carriers than the 14:1 sample, but it is also more mobile. Instead, the conductivity is maximized at 14:1 despite the fact that it is semicrystalline at 50 °C and less mobile. We discussed above how the 14:1 sample is structurally unique because it has the largest lamellar spacing, and perhaps this influences the PEO mobility. Our QENS data show that this is not the case, and the maximum conductivity cannot be attributed to fast PEO mobility. Rather, the fast lithium transport must have something to do with the structure of the lamellar phase. As mentioned above, perhaps the lamellae create a directed pathway for lithium transport. Even though this would be useful over small length scales, directed transport must be accomplished over the distance between electrodes for battery operation. These results merit further investigation toward creating directed pathways or networks for lithium ions to travel in SPEs. One modification that might accomplish this is the addition of nanoparticles, which have been shown to improve conductivity.[43] Although the mechanism by which nanoparticles improve conductivity is not clear, it is possible that they create percolated networks, thereby providing a pathway for lithium transport.

Conclusions

We characterize the ionic conductivity, thermal properties, structure, and PEO mobility of semicrystalline and amorphous PEO/$LiClO_4$ as a function of $LiClO_4$ concentration (4:1 to 100:1 and pure PEO). Previous X-ray diffraction results on this SPE show that three crystalline phases can form depending on the lithium concentration: pure PEO, $(PEO)_3$:$LiClO_4$, and $(PEO)_6$:$LiClO_4$. Our DSC results indicate that pure PEO and $(PEO)_3$:$LiClO_4$ crystallize within minutes, whereas the $(PEO)_6$:$LiClO_4$ phase requires days to crystallize. We choose to treat the samples thermally so that only the pure PEO and $(PEO)_3$:$LiClO_4$ crystalline phases are present during the measurements. It is known from previous diffraction investigations that the $(PEO)_3$:$LiClO_4$ phase is formed by a single PEO chain wrapping around a column of Li^+ ions in a helical structure. The $(PEO)_6$:$LiClO_4$

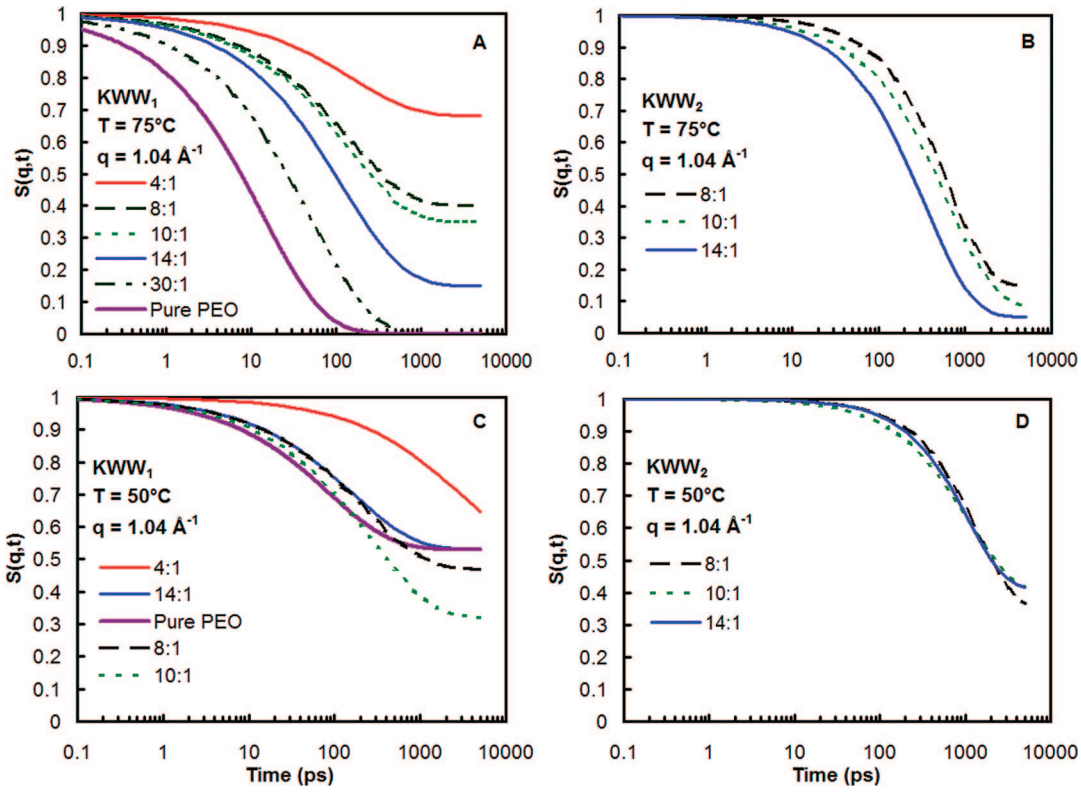

Figure 18. (A) KWW_1 and (B) KWW_2 at 75 °C and (C) KWW_1 and (D) KWW_2 at 50 °C as a function of $LiClO_4$ concentration.

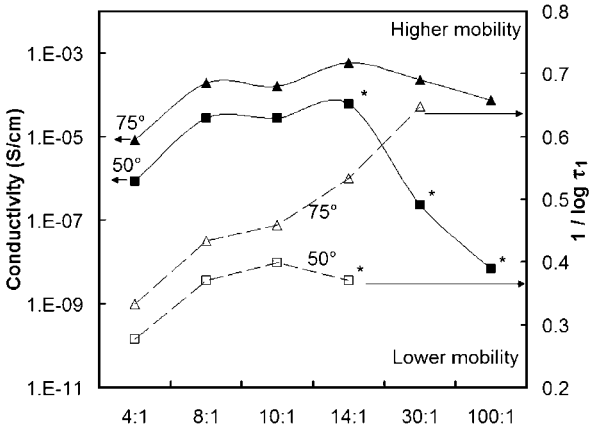

Figure 19. Conductivity and relaxation time as a function of lithium concentration at 75 °C (▲) and 50 °C (■). The data points marked with an (*) designate semicrystalline samples.

phase is similar, except two PEO chains are involved in the formation of the cylinder. This cylindrical structure is known to persist to some extent in the amorphous domain.

We extend the length scale over which structure is investigated by using SANS. Structure is detected by exploiting the scattering length density contrast that results from crystallization. Our results indicate that the $(PEO)_3$:$LiClO_4$ crystalline complex has the morphology of a cylinder with a radius of 125 Å and length of 700 Å. Because the individual cylindrical radius of $(PEO)_3$:$LiClO_4$ is much smaller than this, our result implies that multiple $(PEO)_3$:$LiClO_4$ helices align to form a larger cylindrical structure. In the case of pure crystalline PEO, $LiClO_4$ is expelled from the crystalline regions into the nearby amorphous domains during crystallization, creating contrast between the crystalline lamellae and amorphous PEO/$LiClO_4$ bilayer. Therefore, we are able to detect scattering from crystalline lamellae. We determine that the size of the crystalline lamellae and the amorphous bilayer are maximized at a concentration of 14:1. The conductivity is also maximized at this concentration, despite the fact that the 14:1 sample is semicrystalline and has fewer charge carriers that other samples that are completely amorphous. The concept of increased conductivity through crystalline SPEs has been previously demonstrated, where conductivity through a fully crystalline SPE was shown to be one order of magnitude higher than that of the amorphous equivalent.

To learn how the conductivity and structure are linked to PEO mobility, we directly measure PEO mobility using QENS. In agreement with previous results, the addition of $LiClO_4$ decreases polymer mobility because of the coordination of Li^+ ions with ether oxygen atoms. In addition to a fast process attributed to the segmental motion of the PEO backbone, we also observe a second process at longer timescales. By modeling the elastic incoherent structure factor as a function of spatial scale, we attribute the second process to restricted rotation of hydrogen atoms. This type of motion is consistent with what might be expected from the cylindrical structures formed by PEO chains wrapping around Li^+ ions in a ratio of 6:1. The radius of the cylinder returned by our fit is consistent with the value measured by diffraction. This second process appears only for SPEs where the 6:1 structure is present (PEO/LiTFSI, PEO/LiBETI, and PEO/$LiClO_4$). It does not appear in the case of PEO/LiI, where the 6:1 structure does not form at any lithium concentration. Instead, the 3:1 phase forms where one PEO chain is involved, and additional coordination is required from two nearby anions. We suggest that rotation is not possible in this case, hence the reason why a second process is not observed.

QENS results also indicate that the mobility is not maximized in the 14:1 sample where conductivity is maximized at 50 °C. This decoupling of ionic conductivity and polymer mobility suggests that perhaps practical conductivity values could be achieved, even in crystalline SPEs. It is possible that the lamellar phase creates directed pathways for lithium transport; however, the long-ranged morphology would need to be controlled for battery operation. The results of this study support further investigation of conductivity through crystalline SPEs.

Acknowledgment. Financial support for this work was provided by the National Science Foundation, Polymers Program, DMR-0706402. This work utilized facilities supported in part by the National Science Foundation under Agreement No. DMR-0454672. We gratefully acknowledge Paul Butler, Boualem Hammouda, and Steve Kline from the NIST Center for Neutron Research for their assistance with SANS measurements and data fitting.

References and Notes

(1) Robitaille, C. D.; Fauteux, D. *J. Electrochem. Soc.* **1986**, *133*, 315–325.
(2) *Polymer Electrolyte Reviews*; MacCallum, J. R., Vincent, C. A., Eds.; Elsevier Applied Science: New York, 1987.
(3) Labreche, C.; Levesque, I.; Prud'homme, J. *Macromolecules* **1996**, *29*, 7795–7801.
(4) Edman, L.; Ferry, A.; Doeff, M. M. *J. Mater. Res.* **2000**, *15*, 1950–1954.
(5) Lascaud, S.; Perrier, M.; Vallee, A.; Besner, S.; Prud'homme, J.; Armand, M. *Macromolecules* **1994**, *27*, 7469–7477.
(6) Mao, G.; Saboungi, M. L.; Price, D. L.; Badyal, Y. S.; Fischer, H. E. *Europhys. Lett.* **2001**, *54*, 347–353.
(7) Mao, G. M.; Saboungi, M. L.; Price, D. L.; Armand, M. B.; Howells, W. S. *Phys. Rev. Lett.* **2000**, *84*, 5536–5539.
(8) Londono, J. D.; Annis, B. K.; Habenschuss, A.; Borodin, O.; Smith, G. D.; Turner, J. Z.; Soper, A. K. *Macromolecules* **1997**, *30*, 7151–7157.
(9) Mos, B.; Verkerk, P.; Pouget, S.; van Zon, A.; Bel, G. J.; de Leeuw, S. W.; Eisenbach, C. D. *J. Chem. Phys.* **2000**, *113*, 4–7.
(10) Mao, G. M.; Perea, R. F.; Howells, W. S.; Price, D. L.; Saboungi, M. L. *Nature* **2000**, *405*, 163–165.
(11) Triolo, A.; Arrighi, V.; Triolo, R.; Passerini, S.; Mastragostino, M.; Lechner, R. E.; Ferguson, R.; Borodin, O.; Smith, G. D. *Physica B* **2001**, *301*, 163–167.
(12) Capiglia, C.; Imanishi, N.; Takeda, Y.; Henderson, W. A.; Passerini, S. *J. Electrochem. Soc.* **2003**, *150*, A525−A531.
(13) Gadjourova, Z.; Andreev, Y. G.; Tunstall, D. P.; Bruce, P. G. *Nature* **2001**, *412*, 520–523.
(14) Andreev, Y. G.; Bruce, P. G. *J. Phys.: Condens. Matter* **2001**, *13*, 8245–8255.
(15) MacGlashan, G. S.; Andreev, Y. G.; Bruce, P. G. *Nature* **1999**, *398*, 792–794.
(16) Gadjourova, Z.; Marero, D. M.; Andersen, K. H.; Andreev, Y. G.; Bruce, P. G. *Chem. Mater.* **2001**, *13*, 1282–1285.
(17) Borodin, O.; Smith, G. D. *Macromolecules* **2006**, *39*, 1620–1629.
(18) Staunton, E.; Andreev, Y. G.; Bruce, P. G. *Faraday Discuss.* **2007**, *134*, 143–156.
(19) Andreev, Y. G.; Lightfoot, P.; Bruce, P. G. *Chem. Commun.* **1996**, 2169–2170.
(20) Marzantowicz, M.; Dygas, J. R.; Krok, F.; Nowiński, J. L.; Tomaszewska, A.; Florjańczyk, Z.; Zygadło-Monikowska, E. *J. Power Sources* **2006**, *159*, 420–430.
(21) Marzantowicz, M.; Dygas, J. R.; Krok, F.; Florjańczyk, Z.; Zygadło-Monikowska, E. *Electrochim. Acta* **2007**, *53*, 1518–1526.
(22) Inaguma, Y.; Chen, L. Q.; Itoh, M.; Nakamura, T. *Solid State Ionics* **1994**, *70*, 196–202.
(23) Briant, J. L.; Farrington, G. C. *J. Solid State Chem.* **1980**, *33*, 385–390.
(24) Wunderlich, B. *Macromolecular Physics*; Academic Press: New York, 1980; Vol. 3.
(25) Kline, S. R. *J. Appl. Crystallogr.* **2006**, *39*, 895–900.
(26) Data Acquisition and Visualization Environment (DAVE). http://www.ncnr.nist.gov/dave.
(27) Sakai, V. G.; Chen, C. X.; Maranas, J. K.; Chowdhuri, Z. *Macromolecules* **2004**, *37*, 9975–9983.
(28) Griffith, W. L.; Triolo, R.; Compere, A. L. *Phys. Rev. A* **1987**, *35*, 2200–2206.
(29) Annis, B. K.; Badyal, Y. S.; Simonson, J. M. *J. Phys. Chem. B* **2004**, *108*, 2554–2556.
(30) Chen, Y.; Zhang, Y. H.; Zhao, L. J. *Phys. Chem. Chem. Phys.* **2004**, *6*, 537–542.
(31) Nallet, F.; Laversanne, R.; Roux, D. *J. Phys. II* **1993**, *3*, 487–502.
(32) Beekmans, L. G. M.; van der Meer, D. W.; Vancso, G. J. *Polymer* **2002**, *43*, 1887–1895.
(33) Pedersen, J. S.; Schurtenberger, P. *Macromolecules* **1996**, *29*, 7602–7612.
(34) Chen, W. R.; Butler, P. D.; Magid, L. J. *Langmuir* **2006**, *22*, 6539–6548.
(35) Lightfoot, P.; Mehta, M. A.; Bruce, P. G. *J. Mater. Chem.* **1992**, *2*, 379–381.
(36) Larson, A. C.; Von Dreele, R. B. *GSAS: General Structure and Analysis System*; *Technical Report LAUR-86-748*; Los Alamos National Laboratory: Los Alamos, NM, 1987.
(37) Lightfoot, P.; Mehta, M. A.; Bruce, P. G. *Science* **1993**, *262*, 883–885.
(38) Mao, G. M.; Saboungi, M. L.; Price, D. L.; Armand, M.; Mezei, F.; Pouget, S. *Macromolecules* **2002**, *35*, 415–419.
(39) Jin, X.; Zhang, S. H.; Runt, J. *Polymer* **2002**, *43*, 6247–6254.
(40) Saboungi, M. L.; Price, D. L.; Mao, G. M.; Fernandez-Perea, R.; Borodin, O.; Smith, G. D.; Armand, M.; Howells, W. S. *Solid State Ionics* **2002**, *147*, 225–236.
(41) Sakai, V. G.; Maranas, J. K.; Chowdhuri, Z.; Peral, I.; Copley, J. R. D. *J. Polym. Sci., Part B:Polym. Phys.* **2005**, *43*, 2914–2923.
(42) Bée, M. *Quasielastic Neutron Scattering: Principles and Applications in Solid State Chemistry, Biology, and Materials Science*; Adam Hilger: Bristol, England, 1988.
(43) Croce, F.; Appetecchi, G. B.; Persi, L.; Scrosati, B. *Nature* **1998**, *394*, 456–458.

MA802502U